



Application of DOFS for monitoring post-tensioned anchorage zones in reinforced and fibre reinforced concrete

Downloaded from: <https://research.chalmers.se>, 2025-04-10 18:40 UTC

Citation for the original published paper (version of record):

Gil Berrocal, C., Flansbjer, M., Ekström, D. et al (2025). Application of DOFS for monitoring post-tensioned anchorage zones in reinforced and fibre reinforced concrete. *Journal of Civil Structural Health Monitoring*.
<http://dx.doi.org/10.1007/s13349-025-00937-7>

N.B. When citing this work, cite the original published paper.



Application of DOFS for monitoring post-tensioned anchorage zones in reinforced and fibre reinforced concrete

Carlos G. Berrocal¹ · Mathias Flansbjerg² · Daniel Ekström³ · Rasmus Rempling^{1,4} · Ignasi Fernandez¹

Received: 10 October 2024 / Accepted: 5 March 2025
© The Author(s) 2025

Abstract

Prestressed concrete offers a range of benefits compared to traditional reinforced concrete, but in some markets the application of post-tensioned structures has seen a decline in recent decades. A critical aspect of post-tensioned structures is the design of anchorage zones. This study introduces and evaluates an experimental method based on Distributed Optical Fibre Sensors (DOFS) to assess the behaviour of post-tensioned anchorage zones. Moreover, the effectiveness of steel fibre reinforced concrete (SFRC) is also compared to various setups using conventional reinforcement systems. The aspects analysed include load-deformation behaviour, initial crack formation, and subsequent crack development. The research, based on six tested samples, shows that the application of DOFS in the presented setup holds great potential. Furthermore, the findings indicate that using exclusively SFRC at a volume fraction of 0.5%, without passive reinforcement is not recommended. However, combining SFRC with standard helical reinforcement around the anchorage block appears sufficient to meet desired structural performance, as evidenced by comparisons to control specimens.

Keywords Post-tensioned concrete · Steel fibre reinforced concrete · Distributed optical fibre sensing · Anchorage zone · Digital image correlation · Crack monitoring · Fibre optics

1 Introduction

Compared to traditional reinforced concrete, prestressed concrete offers significant benefits like enhanced control of cracking, reduced deflections, and the capacity for longer spans, along with a more efficient allocation of materials. Prestressed concrete, specifically Post-tensioned Reinforced Concrete (PRC), has been widely implemented globally in many civil engineering projects since its introduction in the 1940s. The application of PRC encompasses large road and railway bridges, nuclear reactors, storage tanks, silos, building floors, and wind turbine foundations. Particularly in the

context of Sweden, from over 2500 bridges maintained by The Swedish Transport administration, nearly 20% of them use post-tensioning technology [1].

Anchorage zones in post-tensioned concrete structures are critical for transferring the large compressive forces introduced by post-tensioning tendons into the surrounding concrete. Anchorage zones, which fall under the category of disturbed regions (D-regions), experience complex stress distributions, with high concentrations of tensile and bursting stresses near the anchorage plates. Properly designed anchorage zones allow the structure to withstand these stresses without cracking or failure, ensuring the durability and integrity of the overall system. However, due to space constraints in reduced cross-sectional areas, congested reinforcement layouts are a common issue that often cause problems while casting and compacting and which can ultimately lead to durability problems and premature failure. Furthermore, complex reinforcement layouts also pose a challenge to accurately estimate stress distributions in anchorage zones [2].

A potential solution to the congested reinforcement layouts, which is now contemplated by the new generation of Eurocodes in the design of anchorage zones, is the partial or

✉ Carlos G. Berrocal
carlos.gil@chalmers.se

¹ Division of Structural Engineering, Chalmers University of Technology, 41296 Göteborg, Sweden

² RISE Research Institutes of Sweden, Chemistry and Applied Mechanics, 50462 Borås, Sweden

³ WSP Sweden, Bridge and Hydraulic Design, Gothenburg, Sweden

⁴ NCC Sverige AB, Drakegatan 10, 41250 Göteborg, Sweden

total substitution of stirrups in favour of fibre reinforcement. Steel fibres have been shown to be a suitable solution to replace conventional reinforcement bars in applications with non-uniform stress fields such as for shear reinforcement [3, 4] and punching reinforcement [5, 6]. Moreover, steel fibres have also been shown to effectively control splitting cracks and even suppress cover spalling [7]. The feasibility of using fibre reinforcement in anchorage zones has previously been investigated, revealing that fibres can help mitigate brittle failure while allowing for a more ductile behaviour with fewer and smaller cracks on the surface, see e.g. [8–10]. However, although there is a general agreement that fibres can reduce the need for secondary reinforcement, there are still discrepancies regarding whether the full replacement of spiral reinforcement and stirrups is feasible [11, 12].

Furthermore, most of the existing research on anchorage zones, either experimental or theoretical, has focused on ultimate load capacity, see e.g. [13, 14], with little attention paid to crack development and the efficiency of reinforcement to arrest crack growth. Additionally, earlier experiments have been conducted using discrete measurement techniques, such as foil strain gauges and displacement transducers, see e.g. [15, 16]. However, discrete sensors offer only limited information about the actual three-dimensional stress distribution in the element and may fail to capture early cracking which develops close to the loading region and propagates later towards the surface.

Hence, the use of advanced monitoring techniques such as Distributed Optical Fibre Sensors (DOFS), applied to these components can lead to new insights and a deeper understanding of their structural performance, as seen in recent works applied to other D-regions [17, 18]. DOFS offer multiple benefits over conventional sensors, including compact size, lightness, resistance to chemical and corrosion degradation, and electromagnetic interference immunity. With recent advancements in optical Rayleigh backscattering reflectometry, there has been a leap forward in the capability to continuously monitor strain along fibre cables with spatial resolutions down to the sub-millimetre scale, providing fresh avenues for performance evaluation. This technology has already been effectively employed in various civil engineering projects, such as monitoring strain in reinforced concrete beams [19–22], and its efficacy in supporting the validation of performance indicators for reinforced concrete elements—specifically in deflection measurement and the identification, location, and measurement of cracks—has been extensively researched and proven [23–25]. DOFS have also been applied in post-tensioned elements for monitoring parameters such as loss of prestressing force, temperature variations, and loss of mechanical anchorage in deteriorated beams. Various DOFS technologies, including Brillouin-based, Rayleigh-based, and Fibre Bragg Grating sensors, have been employed in both short- and long-term studies of

up to 1000 days. However, these applications have largely focused on measuring longitudinal strains, such as in smart strand sensors used to monitor tensioning operations or in-service conditions of prestressed concrete beams [26–31].

As such, the potential of DOFS to monitor PRC structures and assess three-dimensional stress states in anchorage zones remains largely unexplored. A key challenge lies in how to properly deploy DOFS to assess how different passive reinforcement setups or concrete types affect the structural performance of anchorage zones. However, a significant hurdle in the monitoring of these areas is the lack of ready-to-use DOFS-based solutions that can be immediately implemented. As such, this research introduces a method aimed at reliably determining the initiation and growth of cracks induced by prestressing forces applied to concrete elements. Moreover, this study explores experimentally the use of alternate passive reinforcement configurations and two distinct types of concrete: regular concrete and Steel Fibre Reinforced Concrete (SFRC), to elucidate the ability of SFRC to partially replace conventional reinforcement. The experimental data leads to the conclusion that employing DOFS in anchorage areas is possible but requires sophisticated, non-standard solutions for detailed performance assessment. It is also determined that designing anchorage systems using SFRC is a viable option when combined with conventional passive steel reinforcement nearby. However, recommendations against using only steel fibre reinforced solutions are made due to the insufficient ability of steel fibres alone to prevent and manage the progression of cracks.

2 Experimental programme

An experimental campaign was devised to study the behaviour of anchorage zones before and after cracking, as found in post-tensioned reinforced concrete structures, employing DOFS. The design parameters for the test specimens were defined by the constraints of the experimental testing equipment, including maximum size and load capacity, along with the results from preliminary numerical analyses to confirm that the induced cracking load fell within the targeted load range.

2.1 Geometry and reinforcement layout

In this study, the samples were categorized into three different groups with two specimens each: Reference specimens "REF1" and "REF2", "SFRCh1" and "SFRCh2" specimens, and "SFRC1" and "SFRC2" specimens. All groups shared identical external dimensions, i.e. a 300 × 300 mm prism with a height of 450 mm. Each group incorporated a typical anchorage system for post-tensioning, which included the anchor head, the duct coupler, and the duct itself. "REF"

specimens were cast using standard concrete with passive reinforcement configured in accordance with conventional design codes for such cases. Specifically, an external steel cage of stirrups following the specimen outer surface was used, completed by a $\text{\O}10$ mm helical reinforcement with a spiral's diameter of 160 mm surrounding the anchorage device, designed to enhance confinement and mitigate early cracking. The remaining two sample sets, "SFRC" and "SFRCh," were both cast using steel fibre reinforced concrete; their only distinction laid in the arrangement of the additional passive reinforcement. The "SFRCh" specimens utilized the same helical reinforcement surrounding the anchorage device as the reference but without any additional stirrups. On the other hand, the "SFRC" specimens had no additional passive reinforcement to ascertain the effectiveness of the fibres alone in controlling crack propagation. A detailed description and a geometrical breakdown of the examples are presented in Fig. 1.

2.2 Instrumentation

2.2.1 Fibre optics arrangement and support

For the purpose of monitoring the multidimensional strain effects throughout the loading process, fibre optic sensors were installed. For this purpose, a robust fibre optic cable capable of enduring the impacts experienced during casting and load-testing phases was chosen, specifically the BRUS-ens DSS V9 from Solifos with a high grip and a 3.2 mm of outer diameter. This fibre sensor is shielded by a steel tube and a ribbed exterior sheath to enhance strain transfer, and it can measure strains up to 10,000 microstrains ($\mu\epsilon$).

The cables were strategically positioned in a helical manner within the concrete specimens to register tangential strains at various depths. Consequently, this setup allowed the assessment of crack formation, crack propagation and the evaluation of crack widths. It was preferred to embed two helical arrangements of the fibre sensors in each specimen, i.e. one aligned with the internal reinforcing helix and another closer to the surface. Consequently, a custom-designed cable supporting structure was necessary to deploy the sensors in the required positions. This

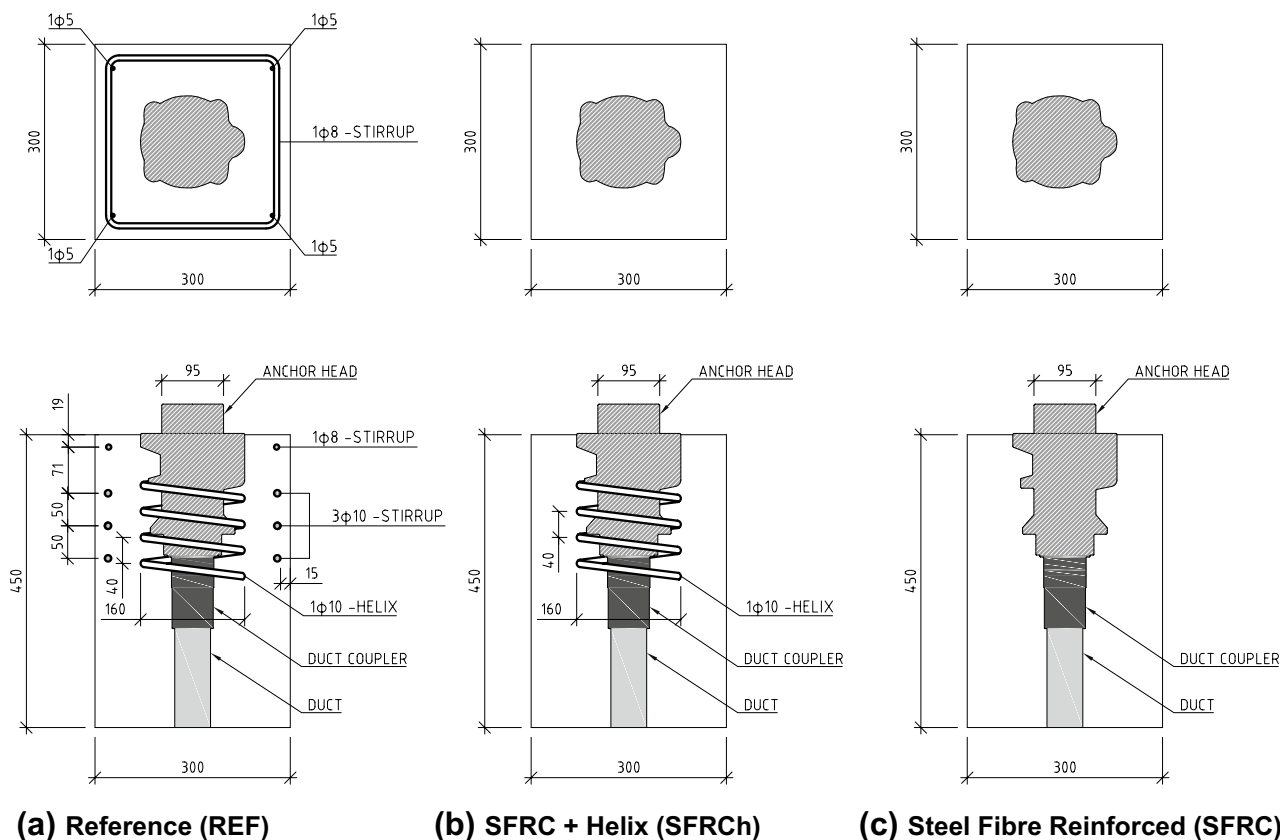


Fig. 1 Geometry of the beam specimen, and reinforcement arrangement: **a** REF specimens, **b** SFRCh specimens and **c** SFRC without additional passive reinforcement

supporting structure consisted of a framework that held the fibre optic cables in place during the concrete casting process. The support was intentionally made with reduced stiffness to minimize the structural influence on the concrete; therefore, plastic material suitable for 3D-printing and precision fabrication was chosen. Moreover, the spiral design aimed at avoiding the segregation of aggregates and steel fibres in the mix. Thus, the spiral was constructed with regularly spaced holes and a specific pitch pattern. To simplify construction, the spiral was made in quarter-circular segments, which could be printed separately and then assembled. Threaded rods with a 5 mm diameter provided external and internal support, connected to the form and anchoring system for the external and internal helices, respectively. To maintain uniform spacing of the sensors, the spiral incorporated a designated notch for the cables, ensuring consistent orientation. The fibre optics' pitch was set at 50 mm per turn for the outer spiral and 40 mm for the inner spiral which mirrors the helical reinforcement's layout. These differing pitches resulted in varied quarter-section heights: 10 mm for the inner spiral and 12.5 mm for the outer. Both spirals had quarter-section thicknesses of 5 mm. Holes were designed with spacings and widths of 5 mm and 2.1 mm, respectively, while the height of the

holes was 7 mm in the outer and 6 mm in the inner quarters, as depicted in Fig. 2.

The helicoid quarters were 3D-printed. The external larger spiral was used for all six samples, and the inner smaller one to simulate the helical support in the two "SFRC" samples, lacking the reinforcement helix. The external spiral involved assembling the 3D-printed quarters as depicted in Fig. 3(a–c), culminating in a spiral of 7.75 turns. The starting point of the first turn was set by adjusting nuts to elevate the base of the first quarter 25 mm from the lower formwork's surface. To keep a consistent 25 mm separation throughout the turns, a tube of that thickness was placed between them. Nuts were also added atop the last turn to secure the structure. This process was similarly employed in constructing the inner spiral, which comprised 4 turns as illustrated in Fig. 3(a–c). Here, the base of the initial quarter was positioned 50 mm from the formwork's bottom, with a constant gap of 20 mm between the turns. After the assembling of the supporting structure the fibre optic was deployed, see Fig. 3(d–f). Further for the specimens retrofitted with helical reinforcement, the DOFS were attached and kept in position by using zip ties, see Fig. 3(d–f).

For the purpose of identifying the position of the fibre optic cables and subsequently correlating the strain

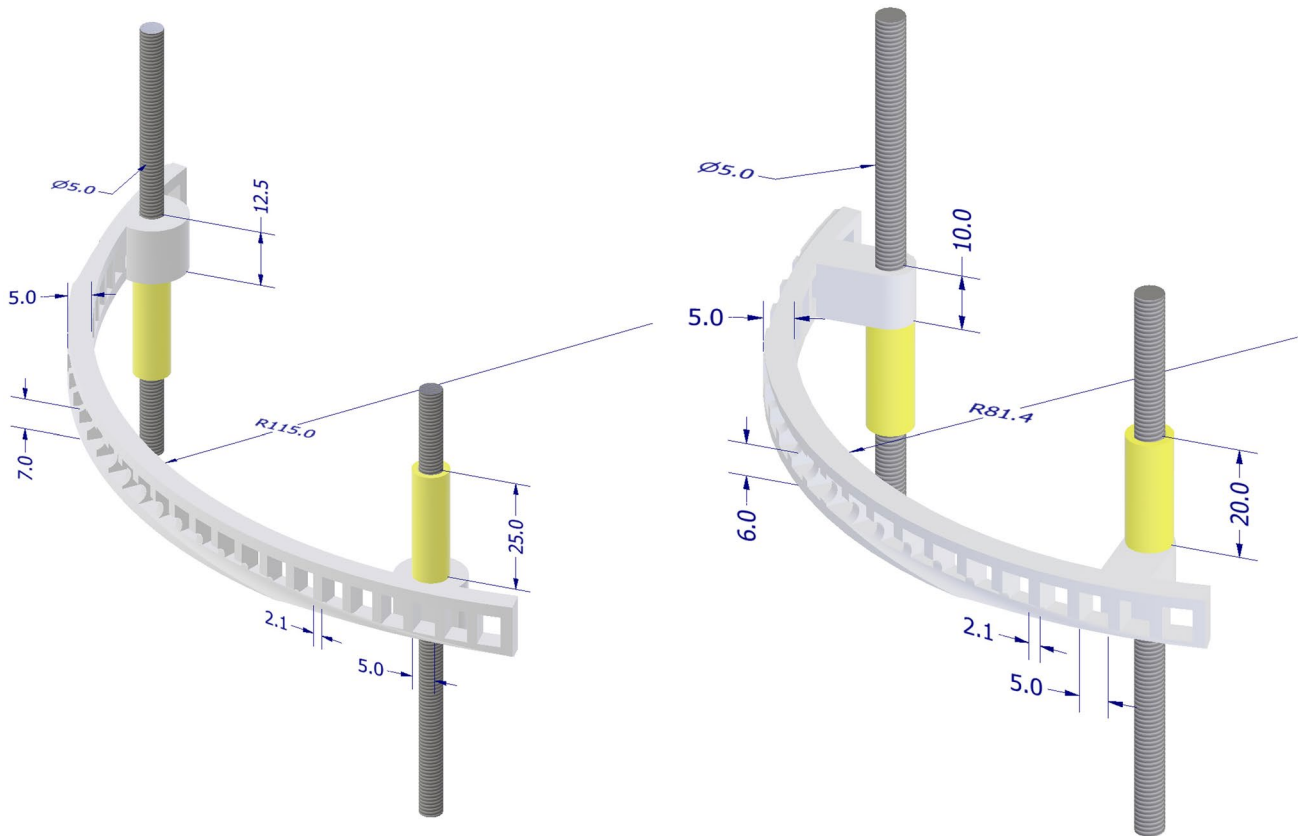


Fig. 2 Geometrical definition of the plastic quarters in the outer and inner spiral. All measurements in mm

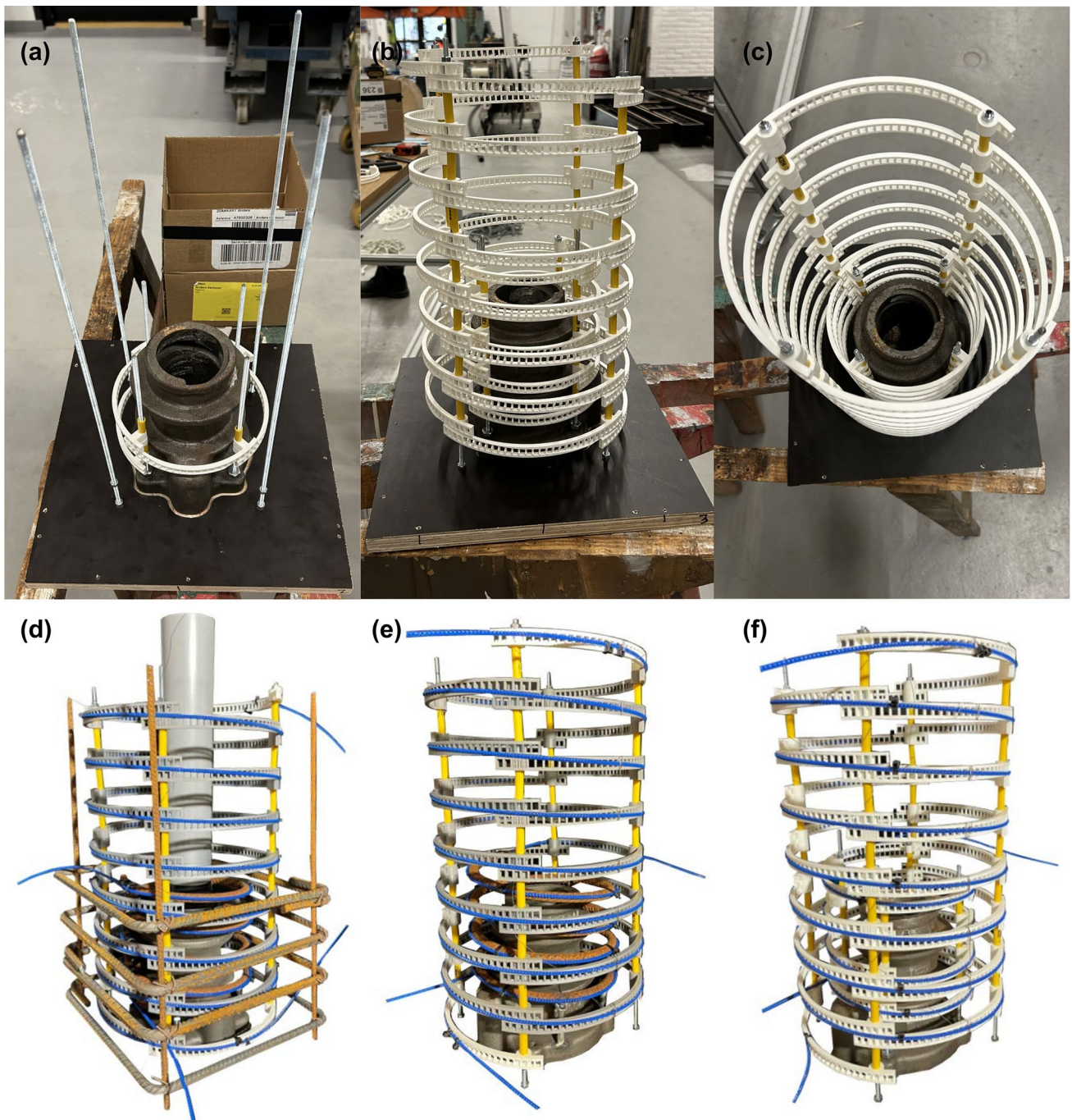


Fig. 3 a–c Support structure for the DOFS attachment. **d, f** DOFS cables attached to the support structure

measurements to a specific location within the test sample, a Kanthal resistance wire was coiled around the fibre optic cable at discrete locations, and for each revolution, for both internal and external helices, ensuring that the wire was always aligned at the same vertical position. When the Kanthal wire was connected to a DC power source, it heated up, and the heat concentrated at the coiled locations, creating distinct thermal strain spikes along the fibre optic cable.

These spikes were easily identifiable in the strain data, serving as reference points for location identification.

The Optical Distributed Sensor Interrogator (ODiSI) 6000 series from Luna Inc. was used as a data acquisition unit. This instrument offers a strain resolution of $1 \mu\epsilon$, a maximum strain range of $\pm 15,000 \mu\epsilon$ and a sample rate that can go up to 250 Hz depending on the gauge pitch, cable and length and number of active channels. In all tests, the largest

available spatial resolution between measuring points provided by the interrogator was chosen, namely 5.2 mm. This configuration provided a combined accuracy (sensor+interrogator) of $\pm 5 \mu\text{e}$, whereas the sample rate was set at 1/3 Hz. It is worth noting a cubic Hermite polynomial interpolation with a spatial resolution of 10 mm was performed on the measured raw data before proceeding to the analysis of the results in order to reduce the data volume without compromising the accuracy.

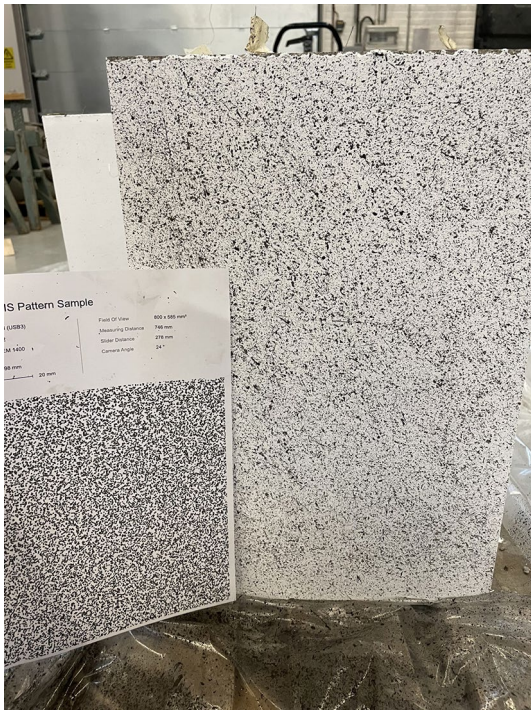
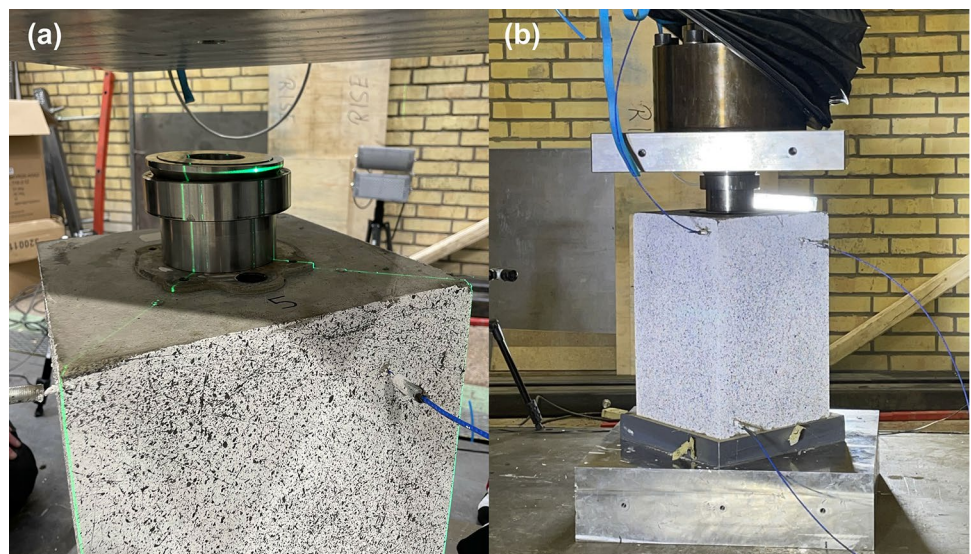


Fig. 4 Speckle pattern used for DIC measurements

Fig. 5 Load set-up and specimen alignment



2.2.2 Digital image correlation (DIC)

To use DIC during the loading of the specimens, a stochastic pattern was generated on the concrete faces. A visualisation of the resulting pattern and comparison with the desired pattern is presented in Fig. 4. Furthermore, four DIC cameras of type CMOS (2048×2448 pixels) were placed perpendicularly at a fixed distance of 0.85 m in front of the specimens' surfaces. The setup yielded a field of view of approximately $350 \times 420 \text{ mm}^2$. White LED light panels illuminated the surfaces to obtain a high contrast in the speckle pattern. The connecting fibre optics cables were arranged to minimise shading the most interesting areas of the surfaces. An image rate of 0.5 Hz was chosen during the load testing. The DIC images from the load testing were post-processed in the Software GOM Correlate to obtain strain fields and crack widths on the surfaces of the specimens. The estimated error associated with the DIC measurements was $\pm 3 \mu\text{m}$.

2.3 Test setup and loading procedure

Specimens underwent concentric load testing in a hydraulic machine with a 1 MN load cell from MFL Prüfsystem, see Fig. 5(a). The load was evenly distributed through a spherical bearing placed on the tendon head. Specimens achieved a flat contact surface using a quick hardening high-strength cement at the machine base. Centrally positioned by lasers, see Fig. 5(a, b), the specimens were tested with a deformation rate of 0.2 mm/min to observe their structural response. Data on load and axial displacement at the anchor head were collected at a 10 Hz sampling rate.

2.4 Material properties of concrete mixes

A self-compacting concrete mix was used to cast the specimens, featuring a concrete strength class C40/50 and a water-to-cement ratio (w/c) of 0.40. The maximum aggregate size was 8 mm and standard Portland cement was used. Following the casting, the specimens were covered with a polyethylene sheet to reduce moisture evaporation and stored in their forms in an indoor climate (20 ± 2 °C and $60 \pm 10\%$ RH) for 7 days. Thereafter, all specimens were stored in water until the age of 28 days when the tests were conducted.

2.4.1 Compressive strength of the concrete mixes

The compression strength of the materials was determined by performing a cube test in accordance with EN 12390–3 [32]. The specimens were successively loaded to failure, and the maximum compression strength was determined. The tests were conducted in a load frame for compressive strength tests provided by Toni technik, model 2040. The loading rate was set to 0.6 MPa/s. All specimens failed according to what is described in EN 12390–3 [32] as a satisfactory failure and the obtained concrete strengths are described in Table 1.

2.4.2 Fracture properties

The fracture properties of the two concrete mixes used, namely plain and fibre reinforced, were determined by performing a wedge splitting test in a test system machine provided by MTS Systems, model 380.10. The test was conducted according to the Wedge Splitting Test Method [33]. To perform the tests, the specimens were cast with a groove on top and equipped with a crack-inducing starting notch that was sawn into the specimen after hardening. In the groove, two metal pieces with roller bearings were placed to pull the specimen apart when the load is applied by a wedge pushed down between the roller bearings. During the test procedure, the Crack Mouth Opening Displacement (CMOD) was

monitored by a clip gauge placed in the groove, which opens when the load is applied. Additionally, the vertical displacement of the wedge and the applied force were monitored during the test procedure. To determine the fracture energy of the materials, the splitting force (F_{sp}) needs to be derived according to Eq. 1.

$$F_{sp} = \frac{F_v}{2 \cdot \tan(\alpha)} \quad (1)$$

where $\alpha = 15^\circ$ is the angle of the wedge and F_v is the applied vertical force.

The fracture energy (G_f) was obtained by integrating the splitting force-CMOD curve and dividing by the ligament area. The maximum CMOD that could be obtained from the clip gauge was approximately 4 mm, and for larger CMOD values, the curve was extrapolated based on the vertical displacement of the wedge and previous CMOD measurements. Figure 6 displays the splitting force-CMOD curve for the three specimens of each material.

Furthermore, the tensile strength of the materials is obtained by analysing the peak splitting force. At the peak, the concrete cracks, and it can be assumed that the cross-section is fully activated and has a linear strain distribution just before the peak value. The tensile strength can then be obtained by moment equilibrium and contribution from the splitting force of the uncracked cross-section. Table 1 lists the fracture energy and tensile strength for each specimen and material.

3 Results

3.1 Load displacement

In the tests, load-shortening behaviour was investigated for each specimen. The specimen's vertical shortening was recorded using the Digital Image Correlation (DIC) system. Initially, a virtual extensometer spanning the entire length of

Table 1 Material properties for the plain concrete and the steel fibre reinforced concrete

Concrete type	Specimen nr	Compressive strength [MPa]	Tensile strength [MPa]	Fracture energy (Gf) [Nm/m ²]	Density [g/cm ³]
Plain concrete	1	39.79	3.53	95.89	2.42
	2	40.94	3.68	114.75	2.41
	3	40.49	3.86	123.02	2.42
	Mean value	40.41	3.69	111.22	2.42
SFRC	1	34.82	3.38	6464.95	2.42
	2	35.46	3.62	3746.08	2.41
	3	35.07	3.21	4235.05	2.42
	Mean value	35.12	3.40	4815.36	2.42

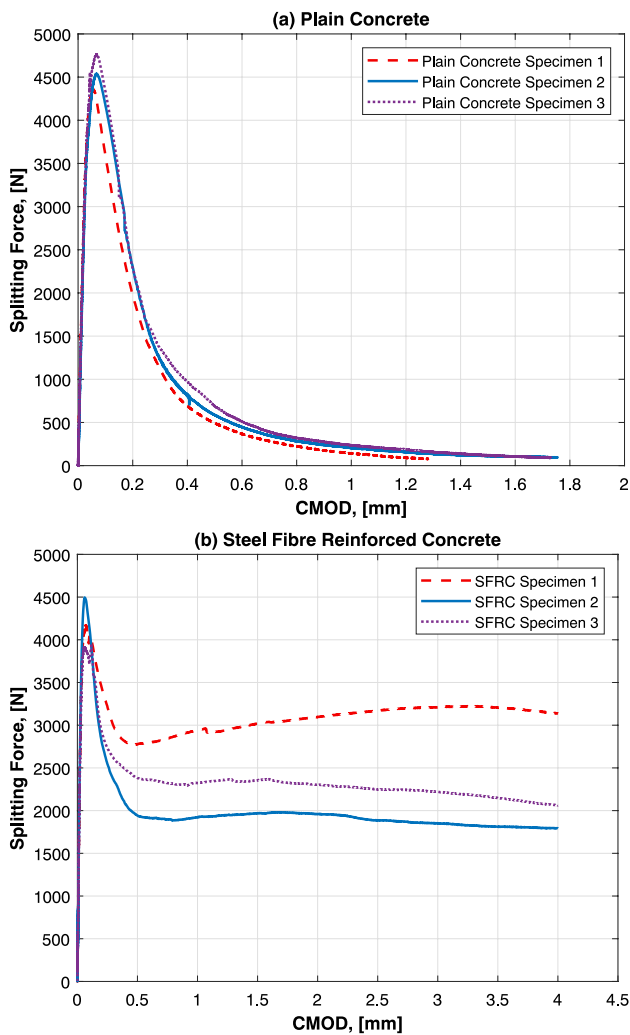


Fig. 6 Splitting force versus CMOD values for both concrete used

the specimen was used to measure total vertical shortening, as illustrated in Fig. 7(a) – Ext-full height. However, initial assessments of the data indicated that due to the centric application of the load on the concrete surface in the test setup, there was an initial uplift of the outer top concrete edges during early load stages, indicating expansion of the specimen as shown in Fig. 7(b). To achieve a more meaningful comparison of the results, the focus was shifted to measuring the vertical shortening within the zone with uniform stress distribution, which was estimated to be approximately located within the 150 mm closest to the concrete base. Thus, twelve virtual extensometers were created, spread out on the four concrete outer faces, with three on each side, positioned two near the edges and one at the centre, as indicated in Fig. 7(a) by Ext – Corner 1, Ext – Corner 2 and Extensometer 2. The average between of the twelve extensometers was calculated for each specimen which yielded the six load-shortening curves presented in Fig. 7(c). As

observed, the displacement applied to all specimens ranged from 0.05 to 0.09 mm, and no significant differences could be discerned between them, given their highly similar overall responses. Analysing in more detail it can be observed that the biggest difference in the curves corresponds to the early load stages, being the behaviour at larger load steps more similar to each other. This initial variation observed at early load level are mostly attributed to the lack of resolution of the measurement equipment as the shortening rates extremely low and any noise in the image or paint pattern may greatly influence the results.

3.2 Distributed optical fibre sensor strain profiles

The DOFS cables recorded strain during the loading of all test samples on both spiral configurations. In order to systematically retrieve and interpret the retrieved data to be plotted in the following sections a schematic description of the sensor breakdown and specimen orientation is provided in Fig. 8.

Figure 9(a–c) depict the resulting strain profiles at a load of 950 kN for REF1, SFRCh1, and SFRC1. The labels 1–4 in these figures correspond to the concrete faces as outlined in Fig. 8. The strain patterns, notable from Fig. 9(a–c), clearly illustrate that, in all cases, peak strains in both the inner and outer spirals are concentrated in the middle of a face. In particular, the highest strains in the outer spiral were noted between revolutions 5–7. Similarly, the peak strains for the inner spiral appeared across all revolutions, with revolutions 1–4 of the inner spiral corresponding vertically with revolutions 5–7 of the outer spiral. For REF1, maximum strain was observed at the centre of face 1, as shown in Fig. 9(a). This distribution of larger strains in the outer spiral is more pronounced at this central point compared to the more evenly spread larger strains of the inner spiral, which appear at both the centre and corners of the specimen. Regarding SFRCh1, as displayed in Fig. 9(b), the highest strain concentrations were found at the centres of faces 2 and 4 for both spirals, potentially due to the symmetry of the specimen influencing the similarity in strain concentration and intensity across these two faces. The localization of strain is noticeably higher in SFRCh1 than in REF1. In addition, the strain profile within the inner spiral of SFRCh1 shows less uniformity when compared with REF1. As observed in Fig. 9(c), SFRC1 has its most significant inner and outer spiral strains centralized at Face 1. Furthermore, differences in the average strains between the inner and outer spirals are more pronounced in SFRC1 compared to REF1 and SFRCh1, with additional minor areas exhibiting high strain, such as the corner junction between Faces 3 and 4; this was not evident in the outer spiral nor observed in REF1 and SFRCh1. This may indicate the presence of a crack that was propagating from the centre but did not reach the concrete surface.

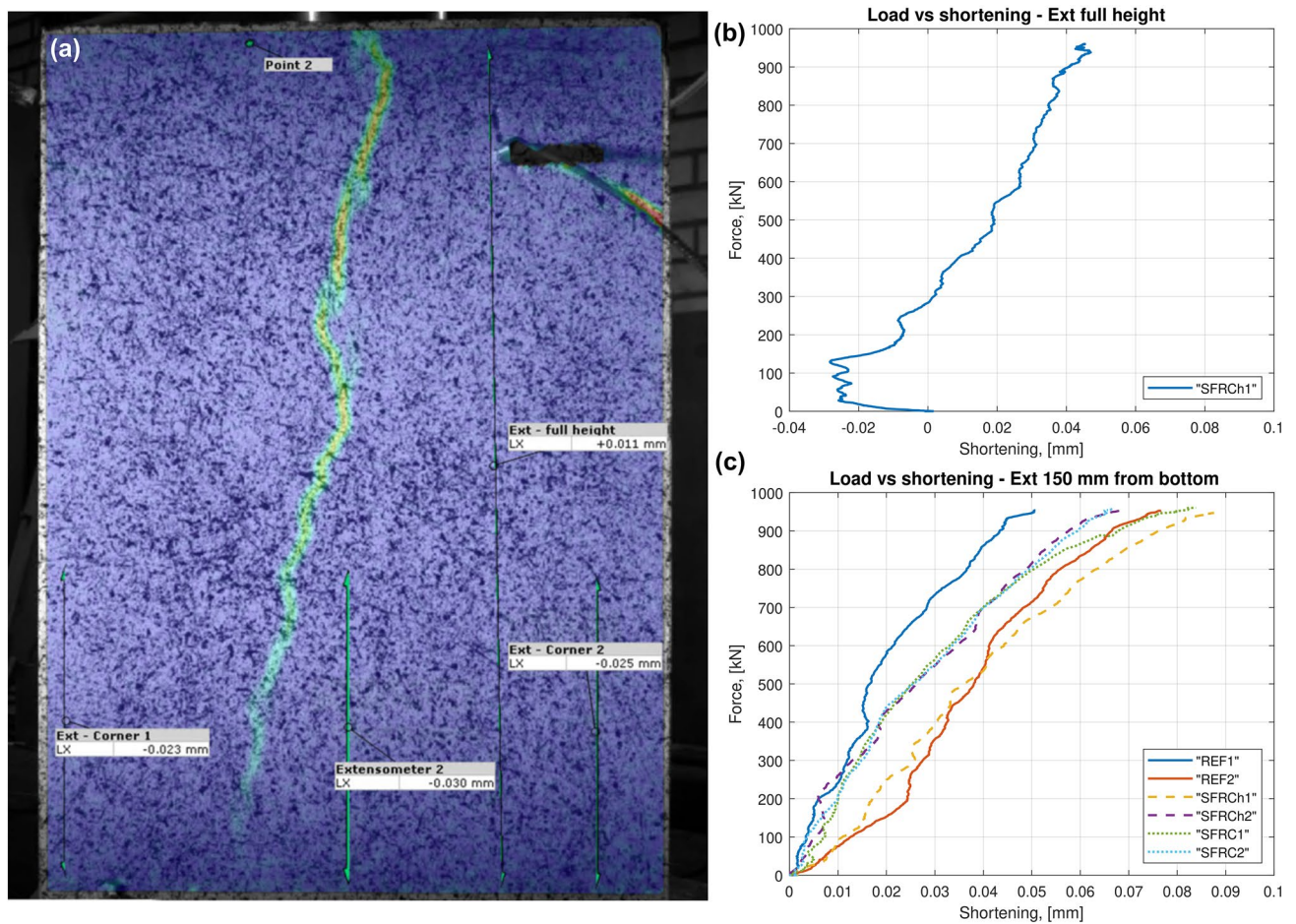


Fig. 7 Set-up of Load-shortening curves obtained from the concentric load testing. The estimated error associated with the DIC measurements was $\pm 3 \mu\text{m}$

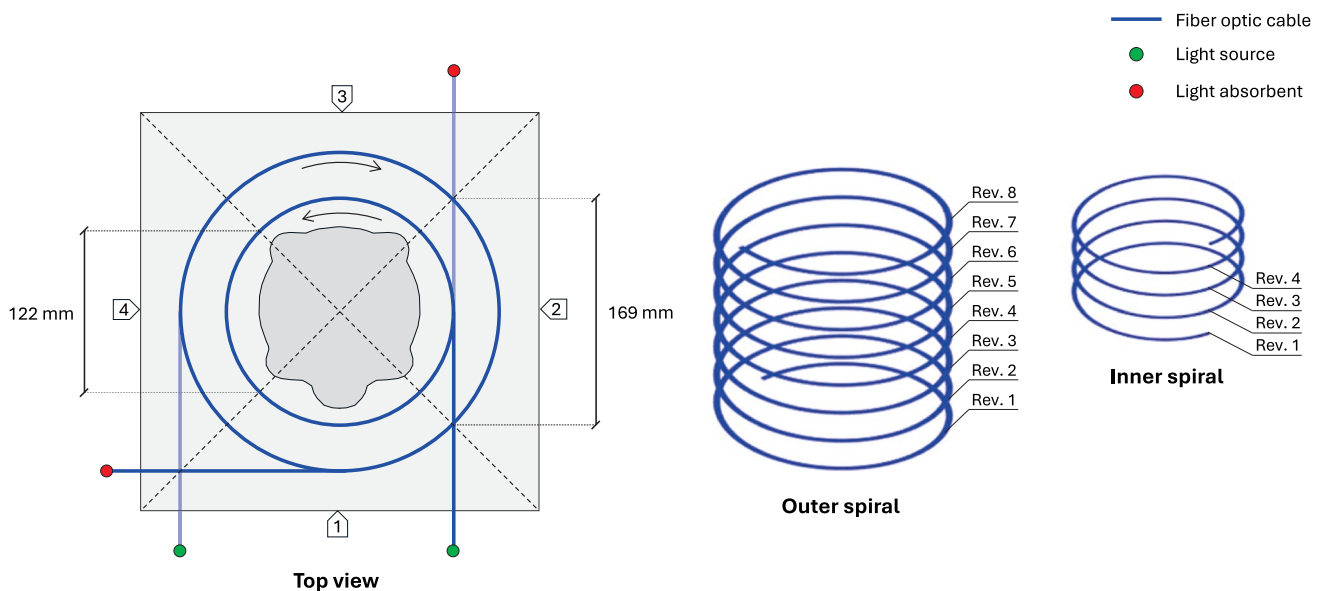


Fig. 8 Nomenclature for data visualization of DOFS data

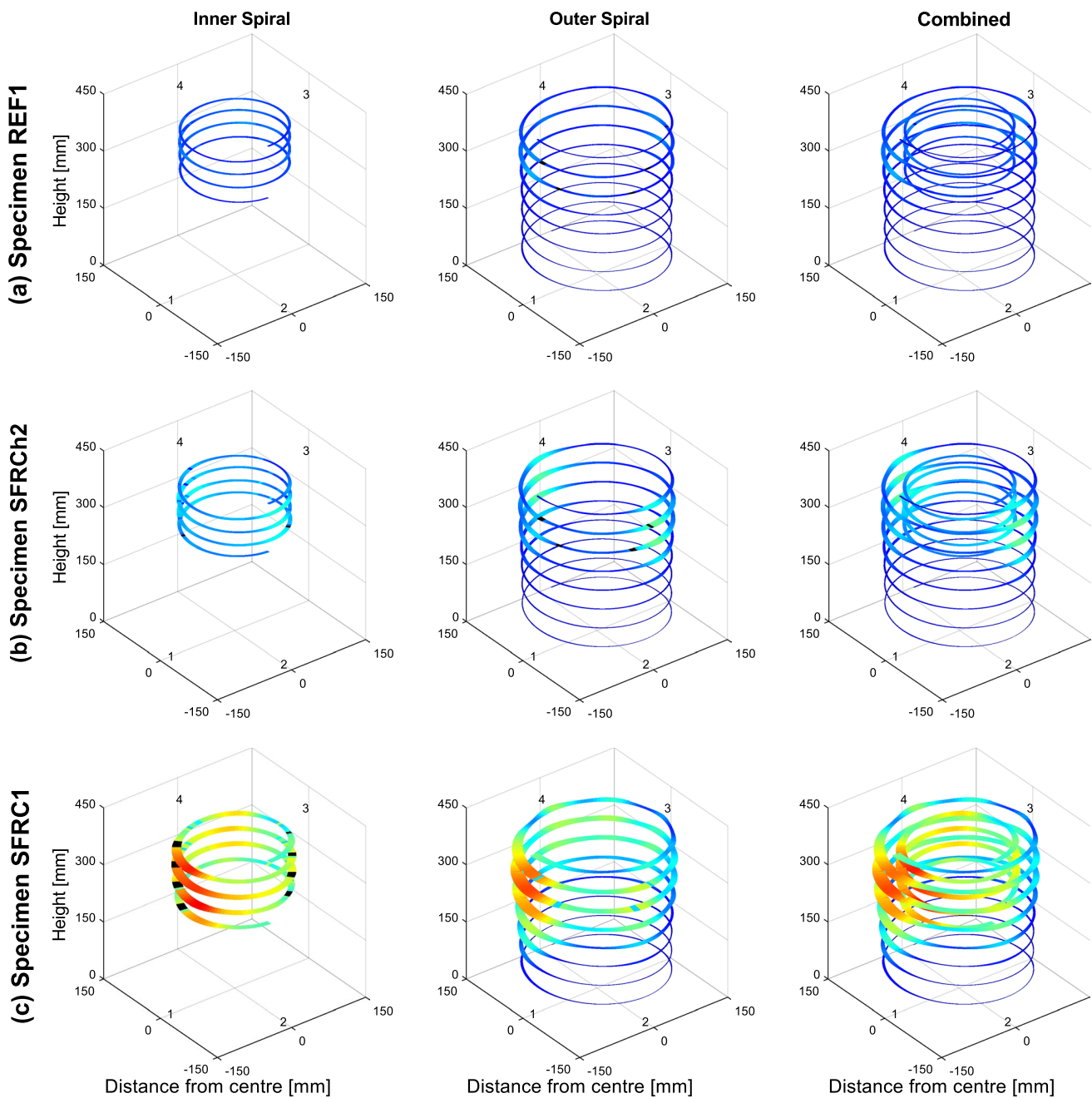


Fig. 9 Strain distribution measured by DOFS at load level 950 kN for specimens **a** REF1, **b** SFRCh1 and **c** SFRC1

3.3 Crack detection and strain localisation

The evolution of the strain profiles during the load tests, as recorded by the DOFS in both the inner and outer spirals, are documented in Fig. 10(a–f). Contrary to Fig. 9, Fig. 10 depicts optic measurements as a continuous line, representing the cable as if it were fully straightened. The figures include annotations of the specimen's face number, and helicoid revolution for easier tracking of the cable's

position within the specimens, with different colours denoting each level of the applied load.

Analysis of the strain patterns along the specimen height reveals that the highest strain levels consistently occur between the 5th and 7th revolutions, corresponding to a vertical span of approximately 225 mm to 375 mm across all load steps (similar to Fig. 9). Notably, the steel fiber-reinforced concrete (SFRC) without additional passive reinforcement exhibits more pronounced strains in the lower

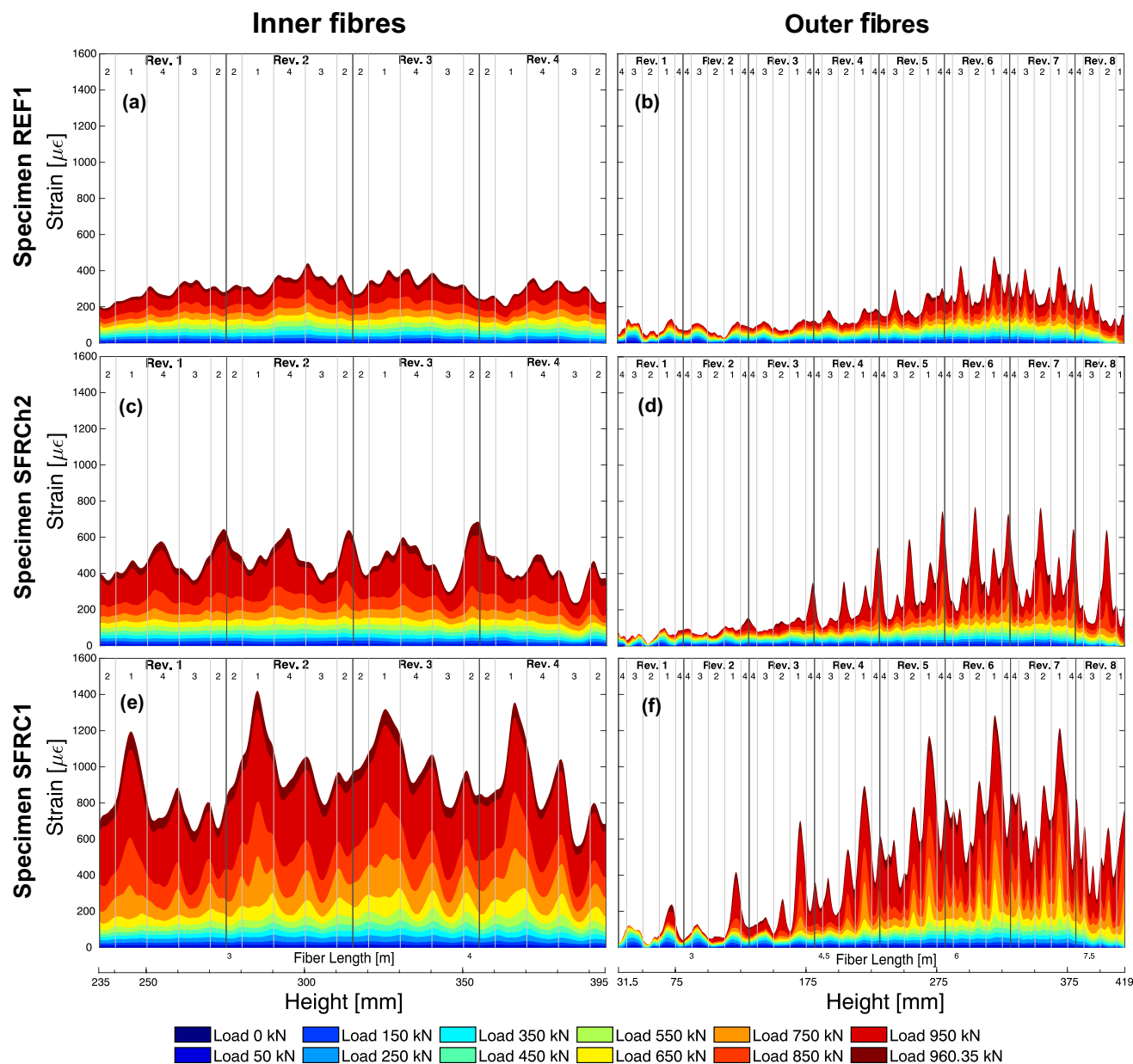


Fig. 10 Strain distribution recorded by DOFS at different load levels for the outer DOFS cable, (a), (c) and (e), and inner DOFS cable, (b), (d) and (e). a, b REF1, c, d SFRC1 and e, f SFRC2

regions of the specimen compared to other configurations, as illustrated in Fig. 10(e–f).

Additionally, strain localization, which indicates cracking, becomes apparent around a load of 500 kN, most notably at face 1 for REF1 and SFRC1, and faces 2 and 4 for SFRC1, as previously seen in Fig. 9. Beyond that load, the strains display a progressive increase alongside the increasing load, where strain localization becomes more accentuated up to the peak load of 950 kN.

The outer spiral of REF1 reflects a strain concentration at the centre of its faces, as shown in Fig. 10(b), where peaks are more prominently located on Face 1. Compared to this,

the inner spiral’s strain profile, as seen in Fig. 10(a), exhibits less central prominence, with strain peaks varying across the specimen. The maximum strains at the peak load of 950 kN result in 446 $\mu\epsilon$ and 458 $\mu\epsilon$ for the outer and inner spirals of REF1, respectively. For SFRC1, with strain peaks located on Faces 2 and 4, see Fig. 10(c) and (d), demonstrate these distributions, where the outer spiral especially seems to favour the mid-face region. Although less frequently, some shifting of strains towards the corners also occurs in the inner spiral, except where some are directed towards the edges. This specimen experiences maximum strains at 950 kN at 722 $\mu\epsilon$ and 611 $\mu\epsilon$ for the outer and inner spirals,

correspondingly. Regarding SFRC1, most faces display centrally located strain peaks as illustrated in Fig. 10(e). However, the inner spiral occasionally shows deviations from this pattern as seen in Fig. 10(f), with the most notable strain peaks over Face 1. The recorded maximum strains for SFRC1 at 950 kN are 1211 $\mu\epsilon$ and 1319 $\mu\epsilon$ for the outer and inner spirals, in that order.

When comparing the effect of having an inner reinforcement helix or not, it can be seen that for SFRC1 the inner spiral bears higher strain values compared to the helix-reinforced designs. Implementing helical reinforcement tends to produce more even strain distributions, yielding marginally higher strain readings closer to the surface. Markedly, SFRC1 demonstrates substantially greater strain than the other specimens in terms of both peak and generalized strain values. Among the three studied setups, the reference configuration exhibited the lowest strain values, due to the contribution of both layers of passive reinforcement.

3.4 Comparison between DOFS and DIC strain fields

In the load testing phase, 2D Digital Image Correlation (2D-DIC) was also utilized to observe each side of every test sample. Figure 11(a–c) displays the strain distribution projected, according to Fig. 8, onto each specimen face, complemented by DIC measurements at a 950 kN load. The vertical observation of the strain profiles along the specimens yields insights consistent with those discussed in Sect. 3.3; the SFRC1 sample exhibited increased strains over much of its height compared to other variants. It was further noted that strain tended to concentrate around the centre on most faces of the specimens.

An analysis of Fig. 10(a), REF1, reveals pronounced strain localization within a vertical range of about 225 mm to 375 mm, which correlates closely with the zone of visible crack formation on the surface; per the DIC, peak surface strain appears at a height of 300 mm. All faces except for Face 4 developed a centrally situated crack, mirroring the trajectory of the maximum strain recorded by the DOFS. Observations from Fig. 10(b), SFRCh1, illustrate notable strain concentration from a point roughly 175 mm up to the uppermost measurement on Face 2 at 410 mm. The extent of crack development corresponds well with the strain localization as indicated by the DOFS. Similar to REF1, the greatest surface strain is noticed at 300 mm height, paired with the max DOFS-measured strain. The most distinct cracking is seen on Faces 2 and 4, with Face 4's crack notably centered. Cracks on Face 1 commence at the 300 mm mark and veer slightly towards the corner at 175 mm, echoing the pattern found on Face 2. Cracks on Face 3 are less marked. In regard to Fig. 10(c), SFRC1, strain concentration is evident throughout the spiral revolutions, conforming with the cracking patterns identified by the DIC. As with prior

samples, the surface displays the highest strain intensity at the 300 mm level, coinciding with peak DOFS strain readings. Clear cracks are observed on all sides, with Faces 1 and 2 experiencing the most prominent cracking. The cracking on Face 1 begins centrally and shifts near the corner, whereas Face 2 maintains central crack positioning along its entire length.

3.5 Crack width evaluation based on DOFS and DIC measurements

The DIC data enabled monitoring of the initiation and growth of surface cracks during the loading process. The highest strains were observed between revolutions 5–7 on the outer spirals, which dictated where the surface cracks were measured. These measurements from DIC can be correlated with those from the DOFS. Based on [23] and further developed in [24, 25], two methods were used to estimate crack width based on DOFS data namely lower and upper bounds, respectively. In each method, it was presumed that strains on the surface corresponded with the crack formation as only one crack appeared per face at those specific heights for every test sample. For the lower bound, outlined in Eq. 2, it was considered that only strains surpassing the concrete's elastic strain contributed to the crack width, disregarding any strain beneath this threshold. Conversely, the upper bound approach described in Eq. 3 accounted for all positive strains toward the crack width. The calculation of crack width using both methods involved the integration of crack strains over the arc length of each face along the outer spiral, illustrated by Fig. 12. The subsequent section differentiates 'calculated crack widths' derived from DOFS data from 'measured crack widths' obtained through DIC analysis. Table 2 presents the Mean Absolute Error (MAE) between calculated and measured crack widths, computed as described in Eq. 4. Among the two approaches, the upper bound yielded the lowest average MAE, with SFRCh1 exhibiting the smallest MAE.

$$w_{cr}^{lb} = \int_{-l_{a,i}/2}^{l_{a,i}/2} \begin{cases} \epsilon^{DOFS}(x) - \epsilon_{crack} \text{ for } \epsilon^{DOFS}(x) \geq \epsilon_{crack} \\ 0 \text{ for } \epsilon^{DOFS}(x) < \epsilon_{crack} \end{cases} dx \quad (2)$$

$$w_{cr}^{ub} = \int_{-l_{a,i}/2}^{l_{a,i}/2} \begin{cases} \epsilon^{DOFS}(x) \text{ for } \epsilon^{DOFS}(x) \geq \epsilon_{crack} \\ 0 \text{ for } \epsilon^{DOFS}(x) < \epsilon_{crack} \end{cases} dx \quad (3)$$

$$MAE = \sum_{i=1}^n \frac{|w_{cr}^{calculated} - w_{cr}^{measured}|}{n} \quad (4)$$

Figure 13(a–c) displays the comparison of crack widths measured using DIC and those determined via DOFS measurements throughout the loading process for REF1, SFRCh1, and SFRC1. For each specimen, the side with the largest

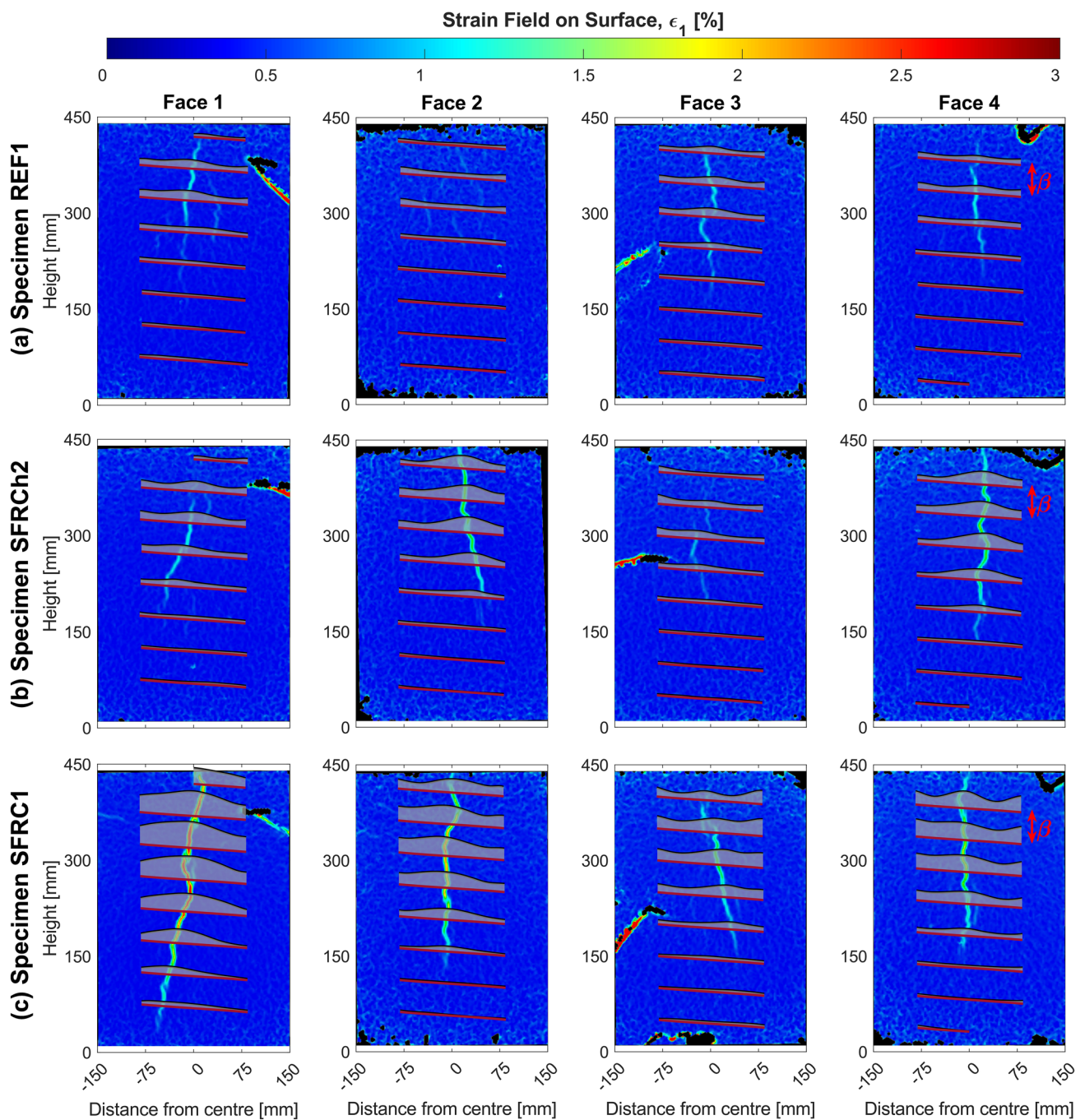


Fig. 11 DOFS strain data projected to the different concrete faces compared to DIC strain fields at 950 kN load level. **a** REF, **b** SFRCh1 and **c** SFRC1

crack was selected for observation: Face 1 for REF and SFRC1, and Face 2 for SFRCh1. The data indicate that the cracks, both measured and calculated, are most prominent at the 6th and 7th revolutions for all specimens. Table 3 shows that the DOFS-measured strains inside the inner spiral surpass the strain capacity of elastic concrete at a lower load level compared to the outer spiral, indicating that cracks start near the inner spiral and extend outward.

Examination of Fig. 13(a–c), REF1, reveals a significant slope shift in the graphs during loading, suggesting the potential formation or expansion of cracks. This reference specimens exhibited the smallest crack widths. As depicted in Fig. 10(a), the widest cracks measured 319 mm at revolution 6, with the largest crack width reaching 0.6 mm under a 960 kN load. The DOFS recorded strains on the spiral's exterior surpassed the expected strain for cracking near 600

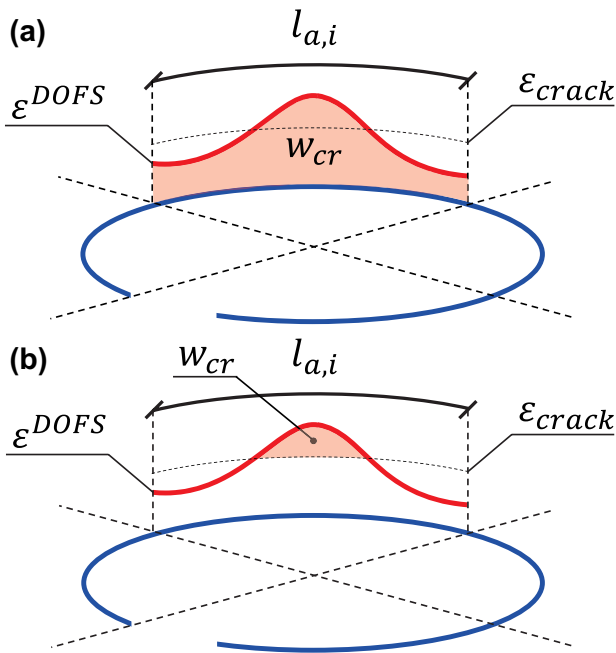


Fig. 12 Strain used in the integration for the calculation of the crack width. **a** Upper bound, **b** Lower bound

Table 2 Mean Absolute Error for the upper and lower bounds calculated crack widths to the measured crack widths, according to Eq. 4

Specimen	Height [mm]	MAE Lower Bound [mm]	MAE Upper Bound [mm]
REF	269	0.017	0.005
	319	0.016	0.003
	369	0.008	0.007
SFRCh1	256	0.004	0.008
	319	0.003	0.011
	369	0.003	0.013
SFRc1	269	0.016	0.009
	319	0.017	0.010
	369	0.013	0.010

kN, and surface cracks became visible around 700 kN. At the onset of cracking, there was no notable alteration in the slope, suggesting consistent crack progression. The crack width measurements coincide more closely with the upper bound approach, which Fig. 13(a) illustrates, and is substantiated by the reduced Mean Absolute Error (MAE) found in Table 2.

Observations from Fig. 13(d–f) indicate that SFRCh1 shares a similar response pattern to REF. Here, DOFS-detected strain levels exceeded the threshold for cracks at roughly 650 kN, with visible surface cracking occurring at 750 kN. Nonetheless, SFRCh1 demonstrated wider cracks

and a significant change in the curve slope occurred at a load of 920 kN, implying accelerated crack growth beyond this point. The maximum crack width was 0.09 mm at a height of 356 mm with a load of 960 kN. According to Fig. 13(d–f), the lower bound approach offers a closer match to the calculated crack widths, with further confirmation from the smaller MAE listed in Table 2.

In SFRc1, Fig. 13(g–i) the broadest cracks were witnessed. Strains gauged by DOFS exceeded those anticipated for cracking around 480 kN, with visual evidence of surface cracking at 600 kN. The crack width trajectories shown in Fig. 13(g–i) are steeper compared to other specimens. The calculated curves exhibit a constant inclination up to 900 kN, after which the crack widths and slopes alter drastically. A similar behaviour is mirrored in the measured data, with an abrupt transition in crack width at 900 kN, succeeded by a tilt change. This may result from a full crack opening and the commencement of fibre pull-out. A load of 960 kN resulted in the highest observed crack width of 0.22 mm at a height of 319 mm (revolution 6). When comparing the measured crack widths to the bound's approaches, there is a marginally better correlation with the upper bound, which is also corroborated by the lower MAE figures in Table 2.

For completeness, selected values of the calculated and measured crack width from the diagrams shown in Fig. 13, have been included in Table 4 to facilitate the comparison of results between the different methods.

4 Discussion

4.1 Evaluation of assessment method

Establishing a method for assessing 3D effects in regions with discontinuities presents multiple challenges. Primarily, it involves developing a support system for the DOFS to monitor complex areas without affecting the anchor zone's structural integrity. Additional considerations must ensure the support does not disrupt DOFS data collection, requiring careful material interaction. Accurate placement of the fibre optics is critical for effective data post-processing, necessitating support stability during casting to accurately pinpoint strain data locations.

The assessment method introduced in this study allows for comparing structural performance across various designs within a discontinuity region. Quantitative analysis of the spiral design's impact on strain measurements and specimen structural behavior cannot be conducted without testing the material and its concrete interface. Nevertheless, the spiral was intentionally designed to minimally affect structural response by selecting a large pitch to prevent segregation and using low-stiffness plastic material. The V9 cable from Solifos, with its rugged surface, was specifically chosen to

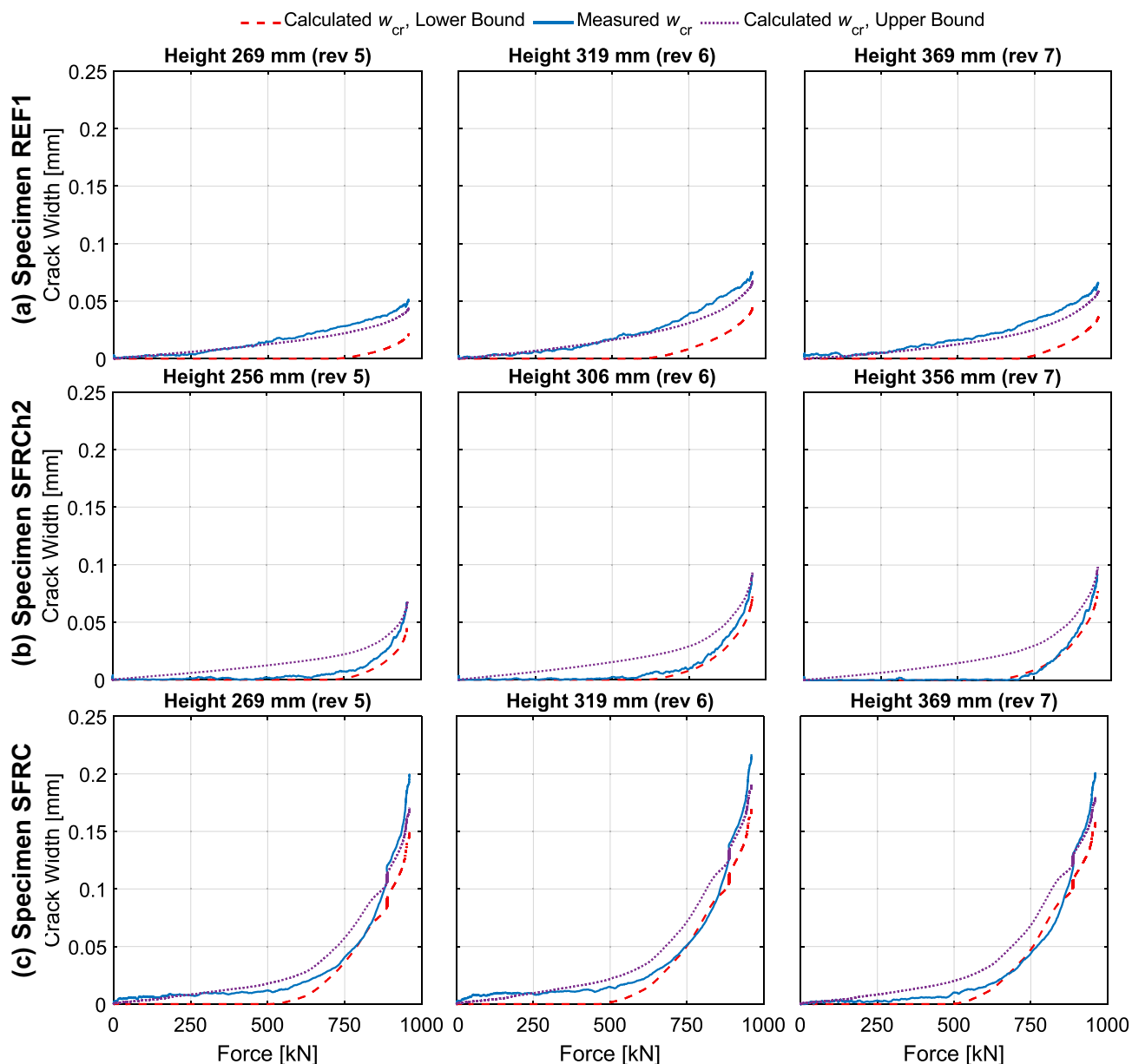


Fig. 13 Comparison of measured crack widths from DIC and calculated crack widths based on DOFS measurement, lower and upper bounds

Table 3 Load level when the recorded strain exceeds the cracking strain at the inner and outer spirals

Specimen	Inner Spiral [kN]	Outer Spiral [kN]
REF1	514	559
SFRCh1	520	591
SFRCh1	377	461

enhance bonding with the concrete, ensuring effective strain transfer and minimizing slip between the sensor and the host material. This bonding mechanism is further reinforced by

the support system's equally spaced holes, which promote mechanical interlock between the concrete and the system, as well as the use of zip ties to secure the fiber optic cables at regular intervals (every quarter of revolution).

Design features like holes in the plastic parts were incorporated not only to enhance concrete bonding but also to more accurately capture concrete strains. During testing, the vertical load applied induced radial compressive stresses, which increased the friction between the sensors and the supporting system, further stabilizing the sensors and reducing slip. It is worth noting that for crack widths below 0.1 mm, the slip between the sensor and the concrete

Table 4 Values of the upper and lower bounds calculated crack widths and the measured crack widths, in μm

	Height [mm]	Force [kN]								
		100	200	300	400	500	600	700	800	900
REF1	269 (rev 5)	0	0	0	0	0	0	0	3	11
		3	3	6	9	15	19	25	32	40
		2	5	7	10	13	16	20	25	33
	319 (rev 6)	0	0	0	0	0	0	5	13	27
		3	5	7	10	17	23	32	45	61
		2	5	8	12	16	21	27	36	50
	369 (rev 7)	0	0	0	0	0	0	0	7	21
		5	3	8	12	17	21	29	38	52
		2	4	6	9	13	16	22	30	43
SFRCh2	269 (rev 5)	0	0	0	0	0	0	0	3	13
		1	1	0	3	5	5	9	44	142
		2	4	7	9	12	16	20	24	35
	319 (rev 6)	0	0	0	0	0	0	3	10	25
		1	3	2	4	6	6	16	60	171
		3	5	8	11	15	19	24	31	46
	369 (rev 7)	0	0	0	0	0	0	4	12	28
		1	2	2	6	10	13	25	76	191
		2	5	7	11	14	19	25	33	49
SFRCh1	269 (rev 5)	0	0	0	0	0	5	23	54	98
		6	8	10	10	12	17	29	55	125
		3	7	10	13	18	25	44	76	120
	319 (rev 6)	0	0	0	0	1	11	34	72	119
		7	10	11	11	15	21	37	67	145
		4	8	12	16	22	32	56	93	141
	369 (rev 7)	0	0	0	0	0	9	32	70	114
		2	2	4	6	10	15	30	59	137
		3	7	10	14	20	31	53	91	135

For each height and load level, the given values correspond, in order, to the lower bound, measured by DIC and upper bound, respectively

is deemed negligible, ensuring reliable strain measurements. By correlating strain patterns from the DOFS with DIC, confirmation that the fibre optics' supporting structure permits evaluating the specimens' structural responses is possible.

There are limitations in the current DOFS design that prevent certain analyses. Since the two spirals differ in pitch, direction, and starting points, comparing their results is impractical. If the spirals shared identical pitch and orientation, the fibre length data would align with the same specimen position. Post-processing encountered issues pinpointing strains due to variations in the helix reinforcement geometry provided by different pitches and diameters. These inconsistencies led to strain localization errors between inner and outer spirals. Unifying helical reinforcement geometries would likely yield improved, consistent results. It is also worth noting that the method presented in this study was mainly developed for laboratory conditions and it was not designed with scalability on mind. While environmental

factors such as temperature fluctuations and chemical exposure might not pose a significant challenge for the application of this method in real-world structures, issues related to space constraints within the formwork, challenges during casting and vibration of the concrete and access to the sensors during the post-tensioning operation arise as critical aspects that could hinder the deployment of this setup in more complex structures.

4.2 Evaluation of anchorage zone's configuration

The results regarding the overall response of the test samples indicate that passive reinforcement does not play a major role in affecting the stiffness, which largely depends on the concrete's cross-sectional area and its modulus of elasticity. Given that the specimen primarily experiences compressive forces, and the passive reinforcement is oriented transversely to the applied load, it has minimal impact on the section's

stiffness. Furthermore, the supplementary capacity due to the confinement added due to the addition of stirrups does not seem to significantly alter the response for the steel configurations used. Therefore, steel fibres appear to provide stiffness comparable to plain concrete with passive reinforcement, but a side-by-side comparison with plain concrete without any reinforcement or only with helical passive reinforcement would be necessary to ascertain the specific contribution of the fibres to overall stiffness. Nevertheless, the data suggests that incorporating steel fibre reinforced concrete in any configuration maintains similar performance levels regarding post-tensioning losses from the concrete's elastic shortening as similar shortening values are measured, an encouraging finding for potential use in future designs.

The structural analysis of the anchorage zones indicates that the SFRC samples underwent the most significant strains and cracks during the loading tests, as detailed in earlier sections. Notably, the greatest strain was observed near the inner spiral of these samples, most probably subjected to larger stresses due to the anchored device. Moreover, the collected data also shows that cracks on the concrete surface were most extensive in the SFRC samples. SFRC tends to exhibit localized cracking in the predicted bursting zone but then extends in an unforeseen manner below it. Once more, the presence of helix reinforcement appears to be quite effective in diminishing both the magnitude of strain and the width of the cracks around the anchorage area, with both spirals presenting strain responses similar to those of the reference samples. This indicates that helical reinforcement is crucial in influencing the cracking process, by reducing strain near the anchorages and restraining crack expansion across the surface, probably because of improved concrete confinement. It is clear that relying solely on SFRC may not adequately control the performance of the structure. A further consistent finding across all samples is that cracking tended to concentrate primarily in the middle of their faces, with Face 1 displaying the most pronounced localization. This pattern could be attributed to the specific design of the anchorage, especially the rounded protrusion towards Face 1 as shown in Fig. 8, which offers the least concrete cover, thereby leading to a heightened stress concentration on this face and promoting the initiation and spread of cracks.

Further analysis of the DOFS data indicates that multiaxial stresses are present in anchorage zones. Since concrete's strength varies with actual stress states, this can affect how cracks form in these regions. Crack initiation tends to start around the anchorage system as shown in Table 3, spreading towards the specimen surfaces. Larger strains and crack widths are observed about 300 mm high, which is lower than where maximum theoretical tensile stresses occur, possibly because of the anchorage system's ribs and depth, leading to a more vertically distributed force within the sample than theoretically expected. Consequently, peak strains and crack

widths appear lower down the specimen. Moreover, the presented comparison between DOFS and DIC data, reveals that DOFS provides accurate assessments for detecting the initiation and progression of cracks, as well as locating them within the specimen. This accuracy persists as long as the cracking is confined to a single location, which was true for all specimens tested. Additional investigation into these methods is necessary for scenarios involving multiple cracks on each concrete surface. The discrepancies between the DOFS and DIC data observed in some specimens are associated with the scaling of the DIC images. Since the field view of the camera could not capture the entire surface, the data needs to be scaled accordingly. Subsequently, all images have been uniformly scaled to facilitate post-processing, which may result in some variability in presented results.

5 Conclusions

The study reviewed the effectiveness of SFRC in mitigating crack propagation when compared with plain concrete across various reinforcement setups. For this purpose, a novel evaluation method using DOFS based on Rayleigh backscattering was developed and implemented. This methodology facilitates strain monitoring within the concrete to determine the initiation of cracking, track crack growth, and crack width calculation. The main conclusions from this investigation are outlined as follows:

- This study introduced and effectively validated a support mechanism for accurately attaching DOFS to measure strains within anchorage zone regions. The system ensured precise sensor alignment and provided a reliable depiction of spatial strain distribution.
- DOFS proved effective in describing the structural behaviour of these regions under typical load conditions.
- Though the bond between the concrete and the DOFS cable may be influenced by the supporting system, the implemented technique appeared to be sufficient for identifying cracks thanks to distinct strain localization. Moreover, it was determined that DOFS are good at detecting not only the initial stages of cracking but also their propagation.
- Using DIC as a reference, the calculated crack widths based on the measured DOFS strains were shown to be very accurate for service loads. Two methods were proposed to calculate an upper and lower bound of the width of cracks crossing the spiral, both yielding values close to those measured by the DIC.
- From a global perspective the use of fibre reinforcement to replace, fully or partially, conventional passive reinforcement did not result in an apparent reduction of global stiffness. Thus, no additional losses associ-

ated with the elastic shortening of the concrete are to be expected or accounted for in new designs based on such material.

- The total replacement of passive reinforcement by steel fibres for volume fractions up to 0.5% is not advisable due to the risk of larger crack widths and extensive crack propagation along the height of the specimens. Nevertheless, conventional skin reinforcement could be potentially replaced with steel fibres without major losses in structural performance given the inner steel helix surrounding the posttensioning device is kept.

Funding Open access funding provided by Chalmers University of Technology.

Data availability The data that support the findings of this study is not publicly available but can be obtained from the authors upon reasonable request.

Declarations

Conflict of interest The authors(s) declared no potential conflicts of interest with respect to the research, authorship and/or publication of this article.

Open Access This article is licensed under a Creative Commons Attribution 4.0 International License, which permits use, sharing, adaptation, distribution and reproduction in any medium or format, as long as you give appropriate credit to the original author(s) and the source, provide a link to the Creative Commons licence, and indicate if changes were made. The images or other third party material in this article are included in the article's Creative Commons licence, unless indicated otherwise in a credit line to the material. If material is not included in the article's Creative Commons licence and your intended use is not permitted by statutory regulation or exceeds the permitted use, you will need to obtain permission directly from the copyright holder. To view a copy of this licence, visit <http://creativecommons.org/licenses/by/4.0/>.

References

1. Trafikverket, BaTMan - Bro och Tunnel Management, (n.d.). <https://batman.trafikverket.se/externportal>.
2. Wollmann G (1992) Anchorage zones in post-tensioned concrete structures, University of Texas at Austin
3. Meda A, Minelli F, Plizzari GA, Riva P (2005) Shear behaviour of steel fibre reinforced concrete beams. *Mater Struct* 38:343–351. <https://doi.org/10.1007/BF02479300>
4. Lim DH, Oh BH (1999) Experimental and theoretical investigation on the shear of steel fibre reinforced concrete beams. *Eng Struct* 21:937–944. [https://doi.org/10.1016/S0141-0296\(98\)00049-2](https://doi.org/10.1016/S0141-0296(98)00049-2)
5. Nguyen-Minh L, Rovňák M, Tran-Quoc T (2012) Punching shear capacity of interior SFRC slab-column connections. *J Struct Eng* 138:613–624. [https://doi.org/10.1061/\(ASCE\)ST.1943-541X.0000497](https://doi.org/10.1061/(ASCE)ST.1943-541X.0000497)
6. Maya LF, Fernández Ruiz M, Muttoni A, Foster SJ (2012) Punching shear strength of steel fibre reinforced concrete slabs. *Eng Struct* 40:83–94. <https://doi.org/10.1016/j.engstruct.2012.02.009>
7. Berrocal CG, Fernandez I, Lundgren K, Löfgren I (2017) Corrosion-induced cracking and bond behaviour of corroded reinforcement bars in SFRC. *Compos B Eng*. <https://doi.org/10.1016/j.compositesb.2017.01.020>
8. Yazdani N, Spainhour L, Haroon S (2002) Application of fiber reinforced concrete in the end zones of precast prestressed bridge girders. <https://www.researchgate.net/publication/242740912>
9. Jalal A, Shafiq N, Zahid M (2019) Investigating the effects of fiber reinforced concrete on the performance of end-zone of prestressed beams. *Materials* 12:2093. <https://doi.org/10.3390/ma12132093>
10. Haroon S, Yazdani N, Tawfiq K (2006) Posttensioned anchorage zone enhancement with fiber-reinforced concrete. *J Bridg Eng* 11:566–572. [https://doi.org/10.1061/\(asce\)1084-0702\(2006\)11:5\(566\)](https://doi.org/10.1061/(asce)1084-0702(2006)11:5(566))
11. Haroon SA, Yazdani N, Tawfiq K (2004) Feasibility of steel fiber concrete in end zones of posttensioned bridge girders : results of special anchorage-device acceptance test. *Transp Res Rec Nat Res Council*. <https://doi.org/10.3141/1892-13>
12. Robinson B, Tawfiq KS, Yazdani N (2009) Using steel fiber reinforced concrete in post-tensioned anchorage zones, in: *Proceedings of the 2009 Structures Congress - Don't Mess with Structural Engineers: Expanding Our Role*. pp. 270–279. [https://doi.org/10.1061/41031\(341\)29](https://doi.org/10.1061/41031(341)29).
13. Pham QQ, Dang NL, Kim JT (2021) Smart PZT-embedded sensors for impedance monitoring in prestressed concrete anchorage. *Sensors*. <https://doi.org/10.3390/s21237918>
14. Yun YM (2005) Evaluation of ultimate strength of post-tensioned anchorage zones. *J Adv Concr Technol* 3:149–159. <https://doi.org/10.3151/jact.3.149>
15. Ro KM, Kim MS, Lee YH (2020) Validity of anchorage zone design for post-tensioned concrete members with high-strength strands. *Appl Sci (Switzerland)*. <https://doi.org/10.3390/app10093039>
16. Ibell TJ, Burgoyne CJ (1993) Experimental investigation of behaviour of anchorage zones. *Mag Concr Res* 45:281–291. <https://doi.org/10.1680/mac.1993.45.165.281>
17. Fernandez I, Berrocal CG, Rempling R (2023) Two-dimensional strain field analysis of reinforced concrete D-regions based on distributed optical fibre sensors. *Eng Struct*. <https://doi.org/10.1016/j.engstruct.2022.115562>
18. Zhang S, Liu H, Darwish E, Mosalam KM, Dejong MJ (2022) Distributed fiber-optic strain sensing of an innovative reinforced concrete beam-column connection. *Sensors*. <https://doi.org/10.3390/s22103957>
19. Barrias A, Casas JR, Villalba S (2019) SHM of Reinforced concrete elements by rayleigh backscattering DOFS. *Front Built Environ* 5:1–14. <https://doi.org/10.3389/fbuil.2019.00030>
20. Rodriguez G, Casas JR, Villalba S (2015) Cracking assessment in concrete structures by distributed optical fiber. *Smart Mater Struct* 24:035005. <https://doi.org/10.1088/0964-1726/24/3/035005>
21. Brault A, Hoult NA, Greenough T, Trudeau I (2019) Monitoring of beams in an RC building during a load test using distributed sensors. *J Perform Constr Facil*. [https://doi.org/10.1061/\(ASCE\)CF.1943-5509.0001250](https://doi.org/10.1061/(ASCE)CF.1943-5509.0001250)
22. Zeng X, Bao X, Chhoa CY, Bremner TW, Brown AW, DeMerchant MD, Ferrier G, Kalamkarov AL, Georgiades AV (2002) Strain measurement in a concrete beam by use of the Brillouin-scattering-based distributed fiber sensor with single-mode fibers embedded in glass fiber reinforced polymer rods and bonded to steel reinforcing bars. *Appl Opt* 41:5105. <https://doi.org/10.1364/AO.41.005105>
23. Berrocal CG, Fernandez I, Rempling R (2020) Crack monitoring in reinforced concrete beams by distributed optical fiber sensors.

- Struct Infrast Eng. <https://doi.org/10.1080/15732479.2020.1731558>
24. Berrocal CG, Fernandez I, Bado MF, Casas JR, Rempling R (2021) Assessment and visualization of performance indicators of reinforced concrete beams by distributed optical fibre sensing. *Struct Health Monit*. <https://doi.org/10.1177/1475921720984431>
 25. Fernandez I, Berrocal CG, Almfeldt S, Rempling R (2023) Monitoring of new and existing stainless-steel reinforced concrete structures by clad distributed optical fibre sensing. *Struct Health Monit* 22:257–275. <https://doi.org/10.1177/14759217221081149>
 26. Gao J, Shi B, Zhang W, Zhu H (2006) Monitoring the stress of the post-tensioning cable using fiber optic distributed strain sensor. *Measurement (Lond)* 39:420–428. <https://doi.org/10.1016/j.measurement.2005.12.002>
 27. Lan C, Zhou Z, Ou J (2012) Full-scale prestress loss monitoring of damaged RC structures using distributed optical fiber sensing technology. *Sensors (Switzerland)* 12:5380–5394. <https://doi.org/10.3390/s120505380>
 28. Huynh T-C, Kim J-T (2017) FOS-based prestress force monitoring and temperature effect estimation in unbonded tendons of PSC girders. *J Aerosp Eng*. [https://doi.org/10.1061/\(asce\)as.1943-5525.0000608](https://doi.org/10.1061/(asce)as.1943-5525.0000608)
 29. Webb GT, Vardanega PJ, Houlton NA, Fidler PRA, Bennett PJ, Middleton CR (2017) Analysis of fiber-optic strain-monitoring data from a prestressed concrete bridge. *J Bridg Eng* 22:05017002. [https://doi.org/10.1061/\(asce\)be.1943-5592.0000996](https://doi.org/10.1061/(asce)be.1943-5592.0000996)
 30. Derkowski W, Sieńko R, Walczak R, Howiacki T, Bednarski Ł (2021) DFOS measurements for strain analysis of anchorage zone in 57-year-old posttensioned precast girder using static and high-frequency approach. *Struct Concrete*. <https://doi.org/10.1002/suco.202100002>
 31. Piątek B, Howiacki T, Siwowski T (2024) Distributed fiber optic sensors for structural health monitoring of post-tensioned bridges. *Bridge Maintenance, Safety, Management, Digitalization and Sustainability - Proceedings of the 12th International Conference on Bridge Maintenance, Safety and Management, IABMAS 2024* 912–920. <https://doi.org/10.1201/9781003483755-106>
 32. EN 12390-3:2009 Testing hardened concrete. Part 3: Compressive strength of test specimens, (2009)
 33. Nordtest, Wedge Splitting Test Method (WST): Fracture testing of fibre-reinforced concrete (MODE I),. (2005).

Publisher's Note Springer Nature remains neutral with regard to jurisdictional claims in published maps and institutional affiliations.